Microbubble dynamics in a viscous compressible liquid near a rigid boundary

Wang, Qian; Liu, Wenke; Leppinen, David; Walmsley, Damian

DOI:
10.1093/imamat/hxz009

Document Version
Peer reviewed version

Citation for published version (Harvard):
Wang, Q, Liu, W, Leppinen, D & Walmsley, D 2019, 'Microbubble dynamics in a viscous compressible liquid near a rigid boundary', *IMA Journal of Applied Mathematics*, vol. 84, no. 4, pp. 696–711. https://doi.org/10.1093/imamat/hxz009

Microbubble dynamics in a viscous compressible liquid near a rigid boundary

Q.X. Wang [a], W.K. Liu [a], D.M. Leppinen [a], A.D. Walmsley [b]

[a] School of Mathematics, University of Birmingham, Edgbaston, Birmingham B15 2TT, UK

[b] School of Dentistry, College of Medical and Dental Sciences, University of Birmingham, Mill Pool Way, Birmingham B5 7EG, UK

This paper is concerned with microbubble dynamics in a viscous compressible liquid near a rigid boundary. The compressible effects are modelled using the weakly compressible theory of Wang & Blake (J. Fluid Mech. 730, 245-272, 2010), since the Mach number associated is small. The viscous effects are approximated using the viscous potential flow theory of Joseph & Wang (J. Fluid Mech., 505, 365-377, 2004), because the flow field is characterized as being an irrotational flow in the bulk volume but with a thin viscous boundary layer at the bubble surface. Consequently, the phenomenon is modelled using the boundary integral method, in which the compressible and viscous effects are incorporated into the model through including corresponding additional terms in the far field condition and the dynamic boundary condition at the bubble surface, respectively. The numerical results are shown in good agreement with the Keller-Miksis equation, experiments and computations based on the Navier-Stokes equations. The bubble oscillation, topological transform, jet development and penetration through the bubble and the energy of the bubble system are simulated and analyzed in terms of the compressible and viscous effects.

1. Introduction

Microbubble dynamics are associated cavitation damage to pumps, turbines and propellers (Blake 1987; Lauterborn & Kurz 2010), as well as applications in biomedical ultrasonics (Coussios & Roy 2007; Curtiss et al. 2013; Wang et al. 2015b; Vyas et al. 2016, 2017), sonochemistry (Suslick 1990; Blake 1999) and cavitation cleaning (Ohl et al. 2006; Reuter et a. 2017).

The boundary integral method (BIM) based on the incompressible potential flow theory is widely used in simulating bubble dynamics (Blake et al. 1986, 1987). Using the BIM the dimension of the problem reduces by one and it thus is grid free in the flow domain and costs less CPU time as compared to the domain approaches. However, the compressible effects of liquid are essential although the associated Mach number is small, which are associated with acoustic radiation at the inception of a bubble and the end of collapse (Prosperetti & Lezzi 1986; Lezzi & Prosperetti 1987).

Viscous effects may be important for very small bubbles (Boulton-Stone & Blake 1993; Wang 2016; Smith et al. 2017). Since the Reynolds number associated is often $O(10)$ or larger, the flow is potential in the bulk volume of the liquid except a thin viscous boundary layer at the bubble surface (Boulton-Stone & Blake 1993).

Transient bubble dynamics considering viscous effects were simulated based on the Navier-Stokes equations using the finite volume method (FVM) (Popinet & Zaleski 2002; Minsier et al. 2009; Hua & Lou 2007) or finite element method (FEM) (Kim et al. 2006; Chen et al.2016). The compressible effects were modelled by Tiwari et al. (2013) and Han et al. (2015) using a diffuse interface model and the FEM, respectively. It is a multi-scaled problem with the thickness of the viscous boundary layer at the bubble surface is small compared with the bubble radius, and both of them change order of magnitude with time. In addition, the wavelength of acoustic waves is in turn much larger than the bubble radius. Simulations of bubble dynamics using FEM or FVM are computationally demanding and are usually carried out for axisymmetric configurations and/or for one cycle of oscillation. Consequently, any theoretical development that can reduce the computational complexity is desirable and thus opening up the opportunity for a relatively simple computational analysis of a wide range of models.

Wang & Blake (2010, 2011) analyzed nonspherical bubble dynamics in a compressible liquid, using the method of matched asymptotic expansions. The flow far away from the bubble is shown to satisfy the linear wave equation to the second order in terms of the Mach number and obtained analytically. The flow near the bubble is shown to satisfy Laplace's equation to second order too. Wang (2013, 2014) showed the computational results based on the weakly compressible theory agreed well with the experiments for underwater explosion bubbles (Hung et al. 2010) and laser generated bubbles near a rigid boundary (Philipp & Lauterborn 1998).

Viscous fluid dynamics can be described approximately by potential flows when the vorticity is small or is confined to a thin viscous boundary layer (Joseph & Wang 2014). It is particularly useful for a gas–liquid two-phase flow with an interface. A key issue in the theory is that the shear stress should approximately vanish at a gas-liquid interface, but it does not in the irrotational approximation. An auxiliary function, the viscous pressure correction to the potential pressure, has been introduced to address this discrepancy by Joseph & Wang (2014). They argued that the power done by the shear stress due to the irrotational flow should be equal to the power done by the viscous correction pressure to conserve the energy of the system. This theory was applied by Lind

& Phillips (2010, 2012, 2013) for bubble dynamics near a boundary based on the BIM, Klaseboer et al. (2011) and Zhang & Ni (2014) for a bubble rising and deforming in a viscous liquid, and Manmi & Wang (2017) for microbubble dynamics subject to ultrasound.

The remainder of the paper is organized as follows. The physical and mathematical model is described in section 2 based on the weakly compressible theory and the viscous potential flow theory coupled with the boundary integral method. In section 3, our numerical model is validated by comparing with the Keller-Miksis equation for a spherical bubble oscillating in an unbounded fluid, the experiment (Philipp & Lauterborn 1998) and the FVM computation (Minsier et al. 2009) for the dynamics of a transient bubble near a rigid boundary. In section 4, we analyze bubble dynamics near a rigid boundary based on the compressible viscous BIM.

2. Physical and mathematical model

Consider the dynamics of a gas bubble near a rigid flat boundary in a viscous and compressible liquid. A Cartesian-coordinate system is set, with the x-axis at the rigid boundary and the z-axis along the axis of symmetry for the configuration, as illustrated in figure 1. It is assumed that it is a potential flow in the bulk volume of the fluid except for a thin viscous boundary layer at the bubble surface.

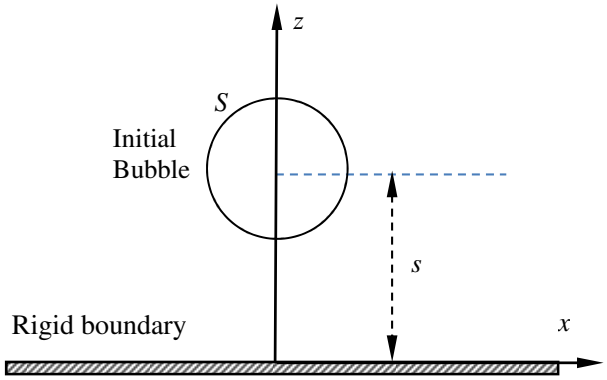

Figure 1. Illustration of a bubble near a rigid boundary, with a standoff distance s from the centre of the initial bubble surface to the boundary, and the coordinates used.

The reference length, density and pressure are chosen as the maximum bubble radius R_{max}, the density of the liquid ρ_∞ in the undisturbed liquid, and $\Delta p = p_\infty - p_v$, respectively, where p_∞ and p_v are the ambient pressure and vapour pressure of the liquid, respectively. The reference velocity is thus obtained as $U = \sqrt{\Delta p / \rho_\infty}$. We introduce dimensionless quantities, denoted by subscripts "*", as follows:

$$\boldsymbol{r}_* = \frac{\boldsymbol{r}}{R_{max}}, \quad t_* = \frac{U}{R_{max}} t, \quad \varphi_* = \frac{\varphi}{R_{max} U}, \quad p_* = \frac{p - p_\infty}{\Delta p}, \tag{2.1}$$

where $\boldsymbol{r} = (x, y, z)$, t is the time, φ the velocity potential and p the pressure of the liquid flow.

The highest speed of the liquid flow induced by bubble dynamics is usually associated with the velocity of the bubble jet, which is often lower than 200 m s^{-1} at normal ambient pressure, as observed in experiments (Benjamin & Ellis 1966, Lauterborn & Bolle 1975, Shima et al. 1981, Tomita & Shima 1986, Vogel et al. 1989, 1990, Lauterborn & Ohl 1997, Philipp & Lauterborn 1998, Lindau, & Lauterborn 2003, Brujan & Matsumoto 2012, Yang et al. 2013; Zhang et al. 2015). **The maximum velocity of the liquid flow associated with the jet occurs locally and for very short period, the velocity during the most time or anywhere else is much smaller than the jet velocity.** As the speed of sound in water is about 1500 m s^{-1}, the flow induced by the bubble dynamics is assumed to be associated with a low Mach number, ε, defined as follows:

$$\varepsilon = \frac{U}{c} << 1, \tag{2.2}$$

where c is the speed of sound of liquid. Lauterborn & Vogel (2013) observed that a newly formed laser bubble's surface expands with an initial velocity of about 2450 ms^{-1}, which decays rapidly to about 250 ms^{-1} within 140 ns.

We divide the bulk fluid domain of the inviscid flow into two regions: the inner region near the bubble where $(x, y, z) = O(R_{max})$ and the outer region far away from the bubble where $(x, y, z) = O(\lambda)$, where $\lambda = cR_{max}/U$ is the wavelength of acoustic waves. Using the method of matched asymptotic expansions, the outer solution was shown to satisfy the linear wave equation to second order in terms of the Mach number and an analytical solution was obtained as follows (Wang 2013, 2014):

$$\varphi_* = -C_0 \frac{\dot{V}_*\left(t_* - \varepsilon r_*\right)}{r_*} + O\left(\varepsilon^2\right), \tag{2.3}$$

where V is the transient bubble volume and C_0 is a given constant with a value of $1/(4\pi)$ and $1/(2\pi)$ for a bubble in an unbounded liquid and near a rigid boundary, respectively.

The inner solution to second order satisfies Laplace's equation and the kinematic boundary condition on the bubble surface, S, as follows (Wang & Blake 2010, 2011):

$$\nabla_*^2 \varphi_* = O\left(\varepsilon^2\right), \tag{2.4a}$$

$$\frac{D\boldsymbol{r}_*}{Dt_*} = \nabla_* \varphi_* + O\left(\varepsilon^2\right) \quad \text{on } S, \tag{2.4b}$$

The far field boundary condition of the inner solution is obtained by matching with the outer solution as follows (Wang 2016):

$$\varphi_* \to C_0\left(\varepsilon\ddot{V}_*(t_*) - \frac{\dot{V}_*(t_*)}{r_*}\right) + O\left(\varepsilon^2\right) \quad \text{as} \quad r_* \to \infty. \tag{2.4d}$$

The initial condition on the boundary is given as

$$\varphi_{n*}\big|_{t_*=0} = -R_{t0*} \quad \text{on} \quad r_* = R_{0*}, \tag{2.4e}$$

where $\boldsymbol{n}$ is the unit normal at the bubble surface pointing to the gas side, R_{0*} and R_{t0*} are the initial radius of the bubble and its initial rate of change, respectively.

A thin viscous boundary layer exists at the bubble surface if the associated Reynolds number is $O(10)$ or larger (Boulton-Stone & Blake 1993). In the viscous potential flow theory, the normal stress balance at the bubble surface, considering the surface tension is given as follows:

$$p_L + p_{\mathrm{vc}} + \sigma\nabla\cdot\boldsymbol{n} - \tau_n = p_B, \ \tau_n = 2\mu\frac{\partial^2\varphi}{\partial^2 n}, \tag{2.5}$$

where p_L is the liquid pressure at the bubble surface, σ surface tension, τ_n the normal viscous stress, p_{vc} viscous pressure correction and μ is viscosity of the liquid.

The tangential stress at the bubble surface should be zero as a result of the relatively low viscosity of the gas inside the bubble. However, the shear stress due to a potential flow is non-zero. Joseph & Wang [1, 34] introduced the viscous pressure correction to resolve the this discrepancy. A rational model for the viscous correction is unavailable at the moment. We assume that the viscous correction pressure p_{vc} is proportional to the normal stress $p_{vc} = -C\tau_n$ (Manmi & Wang 2017)

$$p_L + \sigma\nabla\cdot\boldsymbol{n} - 2\mu(1+C)\frac{\partial^2\varphi}{\partial n^2} = p_B. \tag{2.6}$$

The constant C is to be determined as following. To satisfy energy conservation for the liquid flow, the viscous pressure correction is set to perform the equal power as the shear stress at the free surface, which leads to the following relation at the bubble surface (Joseph & Wang 2004),

$$\int_S u_n(-p_{\mathrm{vc}})\,dS = \int_S \boldsymbol{u}_\tau\cdot\boldsymbol{\tau}_s\,dS, \tag{2.7}$$

where $\boldsymbol{\tau}_s$ is the shear stress at the bubble surface.

Using the Bernoulli equation, the dynamic boundary condition at the bubble surface can be written as

$$\frac{D\varphi_*}{Dt_*} = 1 + \frac{1}{2}\left|\nabla_*\varphi_*\right|^2 - p_{g0*}\left(\frac{V_{0*}}{V_*}\right)^{\kappa} + \sigma_*\nabla\cdot\boldsymbol{n} - \delta^2 z_* + \varepsilon\frac{V_0''(t_*)}{2\pi} - \frac{2(1+C)}{Re}\frac{\partial^2\varphi_*}{\partial n^2} + O\left(\varepsilon^2\right) \text{ on } S, \tag{2.4f}$$

where $p_{g0*} = p_{g0}/\Delta p$ is the initial partial pressure of the bubble gases inside the bubble, V_{0*} is the initial bubble volume, κ the polytropic index of the bubble gas, $\sigma_* = \sigma/(R_{max}\Delta p)$ the surface tension, $\delta = \sqrt{\rho g R_{max}/\Delta p}$ the buoyancy parameter, and $Re = R_0\sqrt{\Delta p\ \rho}/\mu$ the Reynolds number. We assumed in (2.4f) that the expansion and contraction of the bubble gases are adiabatic. We do not

consider the thermal effects associated with this phenomenon, which may reference to (Szeri et al. 2003; Fuster & Montel 2015).

Examining the initial and boundary value problem of (2.4), one can see that the compressible effects to second order appear only in the far field condition (2.4c), and the viscous effects appear in the dynamics boundary condition at the bubble surface (2.4f). As the basic equation is Laplace's equation, this problem can be modeled using the boundary integral method (BIM). The details on the numerical model using the BIM for this problem can be found in (Wang et al. 1996a; Curtiss et al. 2013; Wang 2014).

A nonspherical bubble collapse often leads to the formation of a high speed liquid jet. The jet subsequently impacts the opposite bubble surface and penetrates the bubble, and the liquid domain is then transformed from a singly connected to a doubly connected domain. The solution to a potential problem in a doubly connected domain is non-unique. The doubly connected domain can be made singly connected by, for example, using a branch cut by Best (1993) or a vortex sheet by Zhang, Duncan & Chahine (1993) and Zhang & Duncan (1994). **Here the branch cut is an artificial boundary introduced into the flow domain and across which the potential is discontinuous, the value of this discontinuity being equal to the circulation in the flow.**

Pedley (1968) and Lundgren & Mansour (1991) modeled the dynamics of a bubble torus with a vortex ring inside, started with a circular cross-section. Wang, et al. (1996b, 2005) developed a vortex ring model from these earlier ideas to model the topological transition of a singly connected bubble to a subsequent toroidal bubble. In the vortex ring model, a vortex ring is put inside the toroidal bubble after jet impact. The circulation of the vortex ring is equal to the jump of the potential φ_* across the contact point at the time of jet impact

$$\Gamma_* = \oint_C \nabla_* \varphi_* \cdot d\boldsymbol{r} = \varphi_{N*} - \varphi_{S*}, \tag{2.8}$$

where φ_{N*} and φ_{S*} are potentials at the impact point. Here we assume jet impact occurs at a single point. The potential φ_* is then decomposed as follows:

$$\varphi_* = \varphi_{vr} + \phi, \tag{2.9}$$

where φ_{vr} is the potential of the vortex ring, which can be obtained from the Biot-Savart law (Wang et al. 1996b, 2005; Liu et al. 2016). With the potential jump being accounted for by the vortex ring using (2.9), the remnant potential ϕ is continuous in the flow field and can be simulated using the BIM model.

The mechanical energy of a bubble system consists of the potential energy and the kinetic energy of the bubble system. The potential energy E_P is given as follows (Wang & Manmi 2014)

$$E_{P*} = \frac{p_{g0*} V_{0*}}{\kappa - 1} \left(\frac{V_{0*}}{V_*} \right)^{\kappa - 1} + \sigma_* A_* + V_*, \tag{2.10}$$

where $A*$ is the area of the bubble surface. The reference energy is chose as $R_{max}^3 \Delta p$.

The kinetic energy in the bubble gases is negligible since density of gases are usually three orders of magnitude smaller than liquids. Wang (2015) introduced the local kinetic energy E_{LK} of the liquid flow in the inner asymptotic region Ω_L near the bubble. Ω_L is bounded by the bubble surface S and a large sphere S_∞, with its centre at the centre of the initial bubble surface and with a radius being large compared to the bubble radius and small compared to the wavelength λ of the acoustic wave. The local kinetic energy E_{LK} is given as follows (Wang 2015):

$$E_{Lk^*} = \frac{1}{2}\int_{\Omega_L} \rho_* \left|\nabla_* \varphi_*\right|^2 dV = \frac{1}{2}\oint_{S+S_\infty} \varphi_* \frac{\partial \varphi_*}{\partial n} dS + O(\varepsilon^2) = \frac{1}{2}\oint_S \varphi_* \varphi_{n^*} dS + O(\varepsilon). \tag{2.11}$$

The local energy of a bubble system in a compressible liquid consists of the potential energy E_P and the local kinetic energy E_{LK} as follows:

$$E_{L^*} = E_{P^*} + E_{LK^*} = \frac{p_{g0^*} V_{0^*}}{\kappa - 1}\left(\frac{V_{0^*}}{V_*}\right)^{\kappa-1} + \sigma_* A_* + V_* + \frac{1}{2}\oint_S \varphi_* \varphi_{n^*} dS. \tag{2.12}$$

3. Validations of numerical model

3.1 Comparison with the Keller-Miksis equation

Figure 2 compares the viscous compressible BIM (VCBIM) and the Keller-Miksis equation (KME) for a spherical bubble damping in an infinite liquid. The parameters in calculations are $R_{max} = 6.0$ μm, $\kappa = 1.667$, $\varepsilon = 100$, $p_0 = 101.1$ kPa, $\rho = 1000$ kg/m^3, $p_{a^*} = 0$, $\sigma = 0.073$ N/m and $Re = 60$. The VCBIM agrees well with the Keller-Miksis equation for five cycles of oscillations. Due to the compressible and viscous effects, the bubble undergoes a damped oscillation, with the maximum radius decreasing and the minimum radius increasing with time.

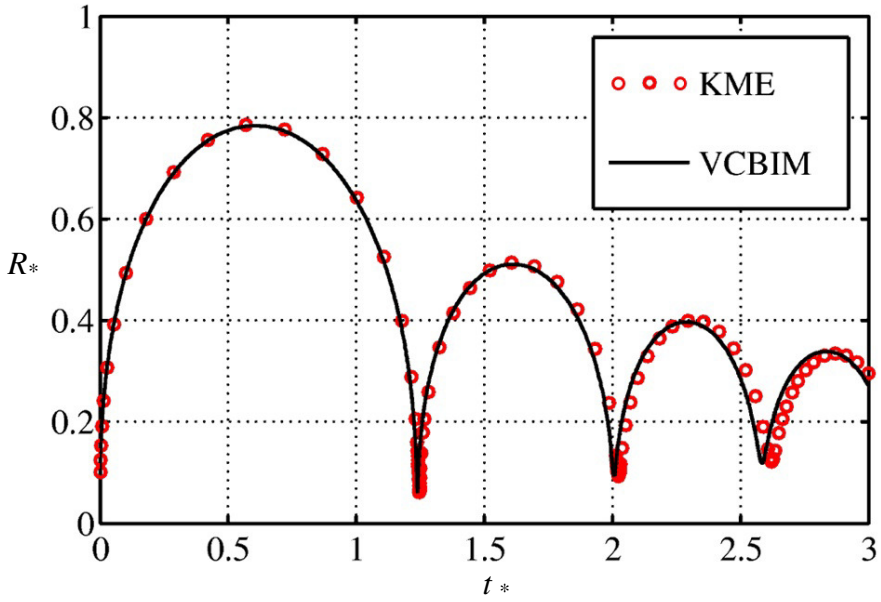

Figure 2. Comparison of the CVBIM and Keller-Miksis equation (KME) for the time histories of the radius R_* for a bubble oscillating in an infinite fluid for $R_{max} = 6.0$ μm, $\kappa = 1.667$, $\varepsilon = 100$, $p_0 = 101.1$ kPa, $\rho = 1000$ kg/m^3, $p_{a^*} = 0$, $\sigma = 0.073$ N/m and $Re = 60$.

3.2 Comparison with the numerical model based on the Navier-Stokes equation

We now compare the computational results of the VCBIM and a numerical model based on the Navier-Stokes equation (Minsier et al. 2009). The case considered is for a bubble collapsing near a rigid boundary with the dimensionless standoff distance $\gamma = s/R_m = 0.9$, in oil with viscosity $\mu = 0.05$ kg/(m s). The Reynolds number for the case is Re = 224. Figure 3 shows the bubble shapes in the collapse phase at typical times, which are noted at the upper-left and upper-right corners of each frame for the numerical model based on the Navier-Stock equation and the VCBIM, respectively. The two models agree well in terms of the bubble shape during the whole cycle of oscillation. A large part of the bubble surface is flattened against the rigid boundary at the maximum volume (see frame 1) and is kept in contact with the boundary subsequently. The top part of the surface collapses down and a jet forms subsequently.

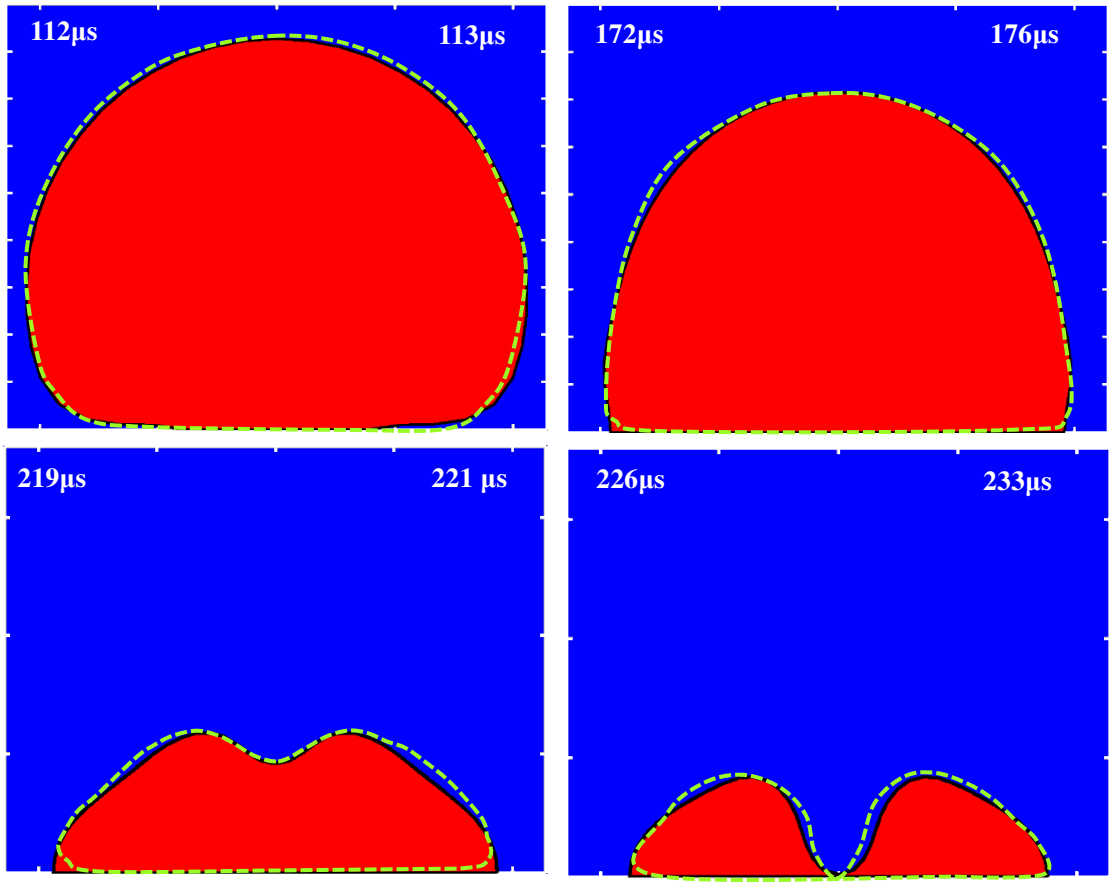

Figure 3. The comparison of the shapes of a bubble near a rigid boundary at $\gamma = 0.6$ calculated using the VCBIM and numerical model based on the Navier–Stokes equation (Minsier et al. 2009) (dash line), in the liquid with viscosity $\mu = 0.05$ kg(m s)$^{-1}$. The rigid boundary is located at the bottoms of the frames. Other parameters are $R_0 = 0.224$ mm, $p_{g0} = 42$ bar, s = 1 mm, p_∞ = 101.3 Kpa, ρ = 998 kg m^{-1} and $\kappa = 1.4$.

3.3 Comparison with experiment results

We next compare the VCBIM with experiments for dynamics of a laser generated bubble with the maximum radius $R_{max} = 1.45$ mm near a rigid boundary with the dimensionless standoff distance $\gamma = s/R_{max} = 0.9$. Other computational parameters are chosen as $\sigma^* = 0.00051$, $\kappa = 1.4$, $R_t^*(0) = 31$, $\varepsilon = 0.013$, $p_{g0^*} = 127$ and $R^*(0) = 0.1$. The corresponding dimensional parameters are $p_\infty = 98.1$ kPa, $p_v = 2.98$ kPa, $\rho = 1000$ kg·m^{-3}, $\sigma = 0.07$ N·m^{-1}, $R(0) = 1.45$ mm, $R_t(0) = 307$ m s^{-1} and $p_{g0} = 12.1$ MPa.

Figure 4 compares the bubble shapes obtained from the VCBIM computation and the experiments (Philipp & Lauterborn 1998), shown on the left and right columns, respectively. In addition, the computational results **(dashed lines)** are added overlapped with the experimental images for a direct comparison. The computation agrees very well with the experiments during the first cycle of oscillation (figure 4A). The expansion of the lower part of the bubble surface is retarded by the boundary at $t = 35$ μs. It approximately takes the shape of half of a sphere at its maximum volume at $t = 177$ μs, with the lower part of the bubble surface being flattened by the boundary. The upper part of the bubble surface then collapses down, taking a cone shape at the middle stage of the collapse phase at $t = 300$ μs. The jet shown in the computational results is not visible in the experimental images due to opaqueness of the bubble surface. Nevertheless, the outer profiles of the bubble obtained in the computation and experiment agree well. The bubble ring of the computation at the end of collapse at $t = 355$ μs agrees well with the experiment, when the bubble reaches its minimum volume.

Figure 4B shows the comparison during the second cycle of oscillation. The bubble surface in the experiments is not clear due to physical instabilities occurred. Nevertheless, the bubble shapes calculated correlate with the experiment data in terms of the outer profile at various times. The bubble ring rebounds and recollapses in contact with the boundary. They agree in terms of the external radius and height of the bubble ring.

A. First cycle of oscillation

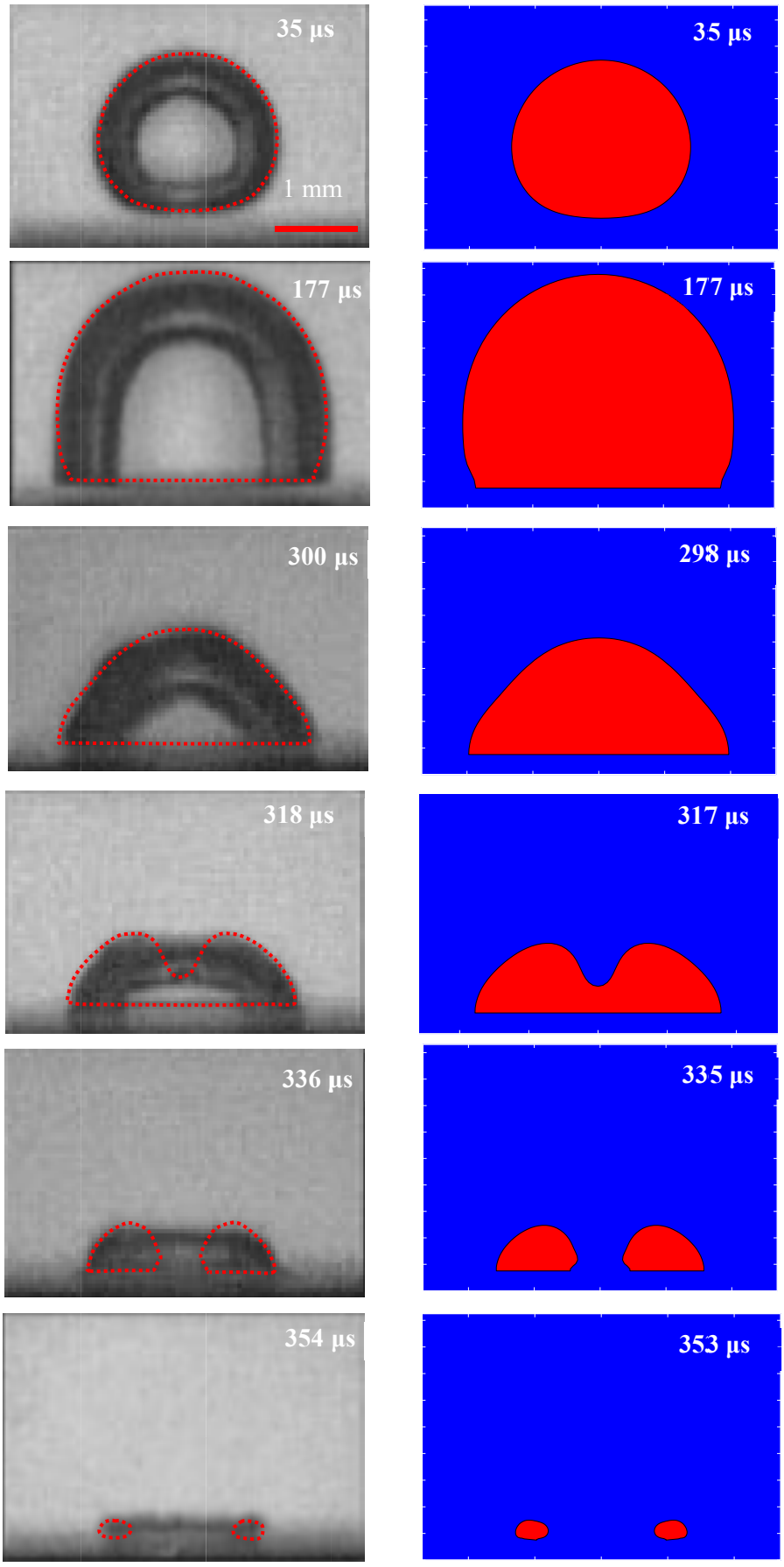

B. Second cycle of oscillation

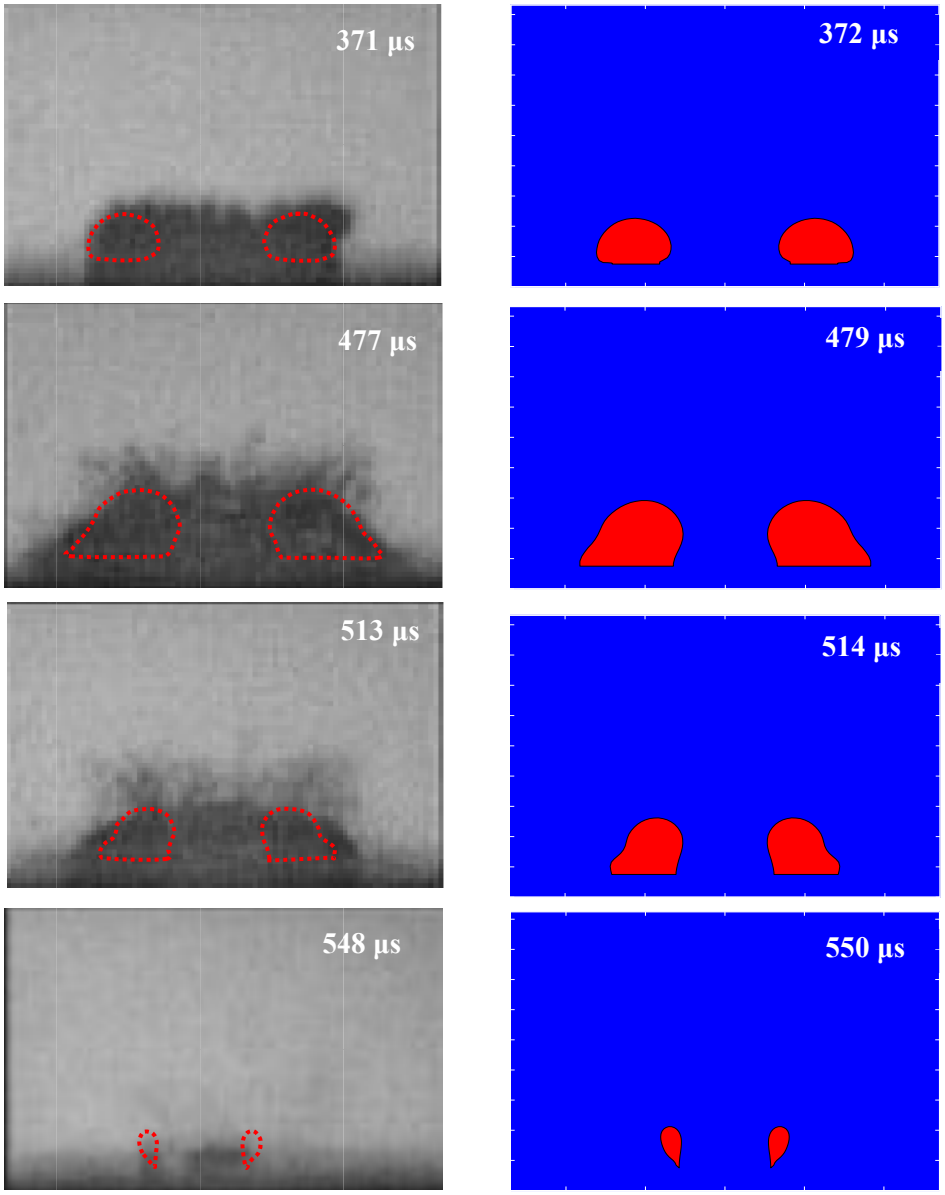

Figure 4. Comparison of the VCBIM computation (right column) with the experiments (left column) (Philipp & Lauterborn 1998) for bubble shapes at various times for a laser-generated bubble near a rigid boundary for $R_{max} = 1.45$ mm and $\gamma = 0.9$, the frame width is 3.9 mm for both results: (A) during the first-cycle and (B) during the second-cycle of oscillation. $\kappa = 1.4$, $\varepsilon = 0.013$, $Re = 1450$, $\sigma_* = 0.00051$, $R_*(0) = 0.1$, $R_{t*}(0) = 31.0$ and $p_{g0*} = 127$.

4. Numerical analyses

The viscous effects are negligible for the case in figure 4 as the associated Reynolds number, $Re = 1450$, is large. To consider the viscous effects, we repeat this case for a microbubble for $R_{max} =$ 6.0 μm, with the associated Reynolds number $Re = 60$ and dimensionless surface tension $\sigma_* = 0.12$. Figure 7 compares the results for $\gamma = 0.6$, and $R_{max} = 6$ μm ($Re = 60$ and $\sigma_* = 0.12$) and $R_{max} = 1.45$ mm ($Re = 1450$ and $\sigma_* = 0.00051$), respectively.

The bubble for $R_{max} = 1.45$ mm expands a longer time to a large maximum volume, having larger part of the bubble surface being flatten by the boundary. During collapse, the bubble collapses towards the boundary and a liquid jet forms on the distal side during the later stage of collapse pointing to the boundary. The bubble for $R_{max} = 1.45$ mm has a large volume before the jet penetrating through the bubble and the jet is sharper. Once it penetrates though the bubble at time of $t_* = 2.11$, 1.67 for $R_{max} = 1.45$ mm, 6.0 μm, respectively, the jet impacts on the boundary immediately. This is associated with higher damage potential as comparing to the damage caused by a bubble jet formed away from the rigid boundary. For the latter case, the jet momentum decreases while penetrating though the liquid before reaching the boundary.

A bubble ring forms after the jet penetrating through the bubble and collapses continuously. After impacting on the boundary, the jet re-directs radically, pushing the inner side of the bubble ring outwards. Meanwhile, the bubble ring collapses from all sides rapidly except for the bottom. When it reaches its minimum volume at $t_* = 2.24$, 1.69 for $R_{max} = 1.45$ mm, 6.0 μm, respectively, the bubble ring in contacting with the rigid boundary reaches the maximum pressure and temperature. This gives rise to another damage potential. In addition, a shock wave is emitted at the minimum bubble volume with high pressure amplitude, it impinges on the rigid boundary once it is emitted and has clear damage potential.

Afterwards, the bubble ring rebounds upwards and outwards along the boundary. It then re-collapses from the top to the bottom and from the external to the internal. The radius of the bubble ring at the end of re-collapse is smaller than that at the end of collapse. The bubble keeps in touch with the boundary during the second cycle of oscillation.

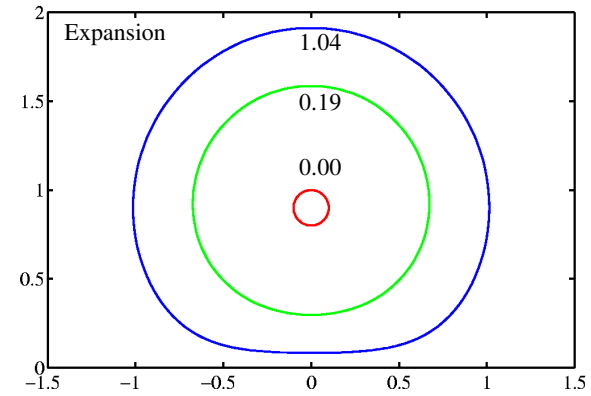
Expansion
1.04
0.19
0.00

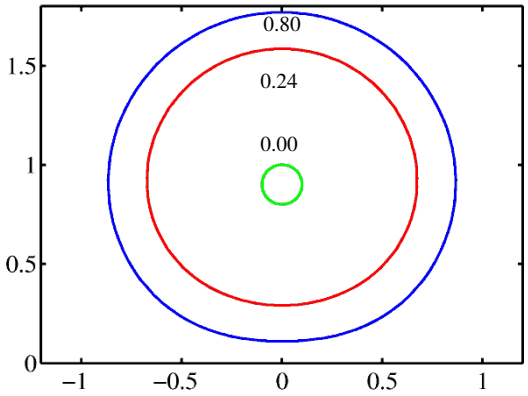
0.80
0.24
0.00

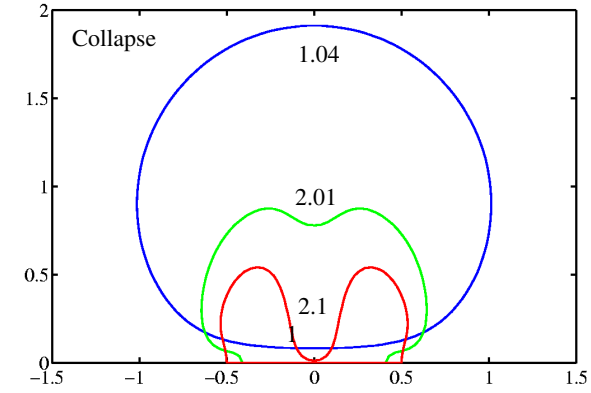
Collapse
1.04
2.01
2.1

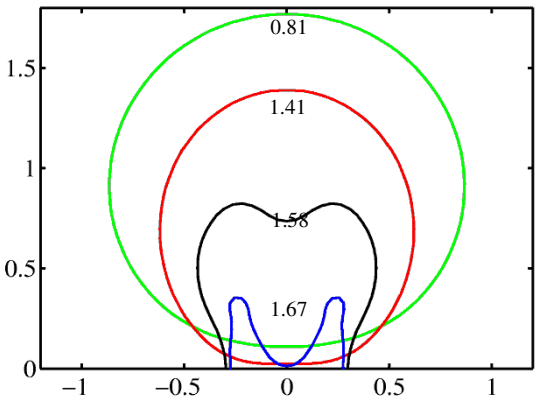
0.81
1.41
1.58
1.67

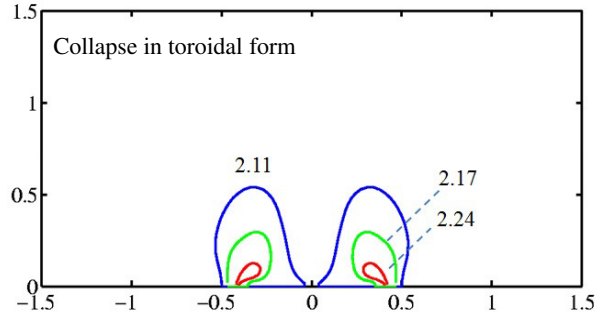
Collapse in toroidal form
2.11
2.17
2.24

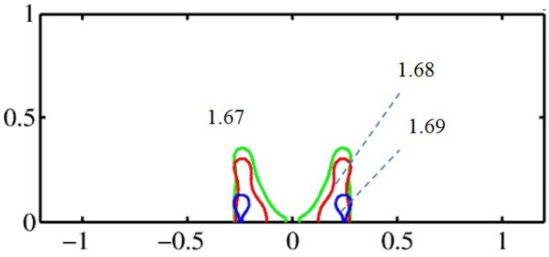
1.68
1.67
1.69

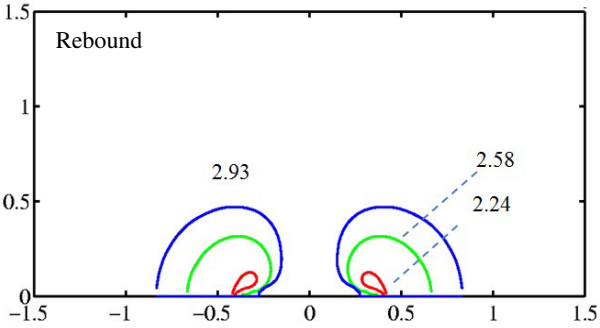
Rebound
2.93
2.58
2.24

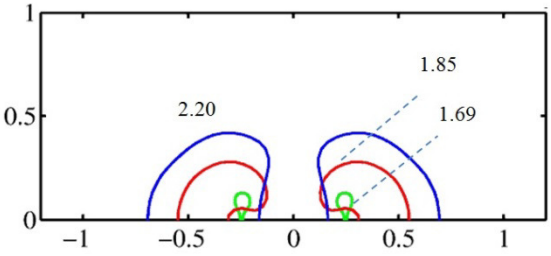
1.85
2.20
1.69

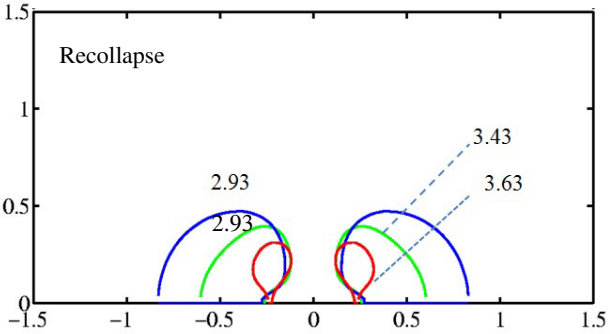
Recollapse
3.43
2.93
3.63
2.93

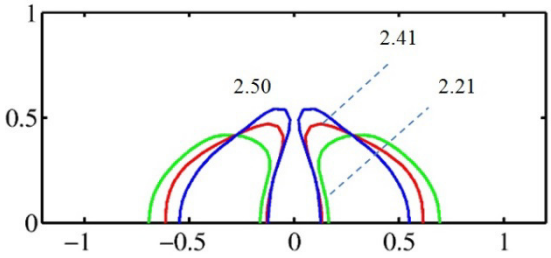
2.41
2.50
2.21

Figure 5. The bubble motion near a rigid boundary for $\gamma = 0.9$, and $R_{max} = 1.45$ mm ($Re = 1450$ and $\sigma_* = 0.00051$) (left column) and $R_{max} = 6$ μm ($Re = 60$ and $\sigma_* = 0.12$) (right column). The remaining parameters are the same as in figure 4.

Figure 6 compares the results for $\gamma = 0.6$, and $R_{max} = 6$ μm ($Re = 60$ and $\sigma_* = 0.12$) and $R_{max} =$ 1.45 mm ($Re = 1450$ and $\sigma_* = 0.00051$), respectively. The bubble for $R_m = 1.45$ mm are associated with a larger maximum volume, a larger part of the surface being flattened by the rigid boundary and a larger volume at the moment of jet impact toward the end of collapse. Once the jet penetrates the bubble for t_* = 2.11, 1.55 for R_{max} = 6 μm, 1.45 mm, respectively, it immediately impacts the rigid boundary. After jet impact, the bubble becomes a bubble ring. It collapses further, reaching the minimum volume at t_* = 2.29, 1.69 for R_{max} = 6 μm, 1.45 mm, respectively, when a shockwave is emitted, which impacts on the rigid boundary immediately. It then rebounds and recollapses, keeping in contact with the rigid boundary. The bubble ring for $R_m = 1.45$ mm has a larger radius and larger maximum volume.

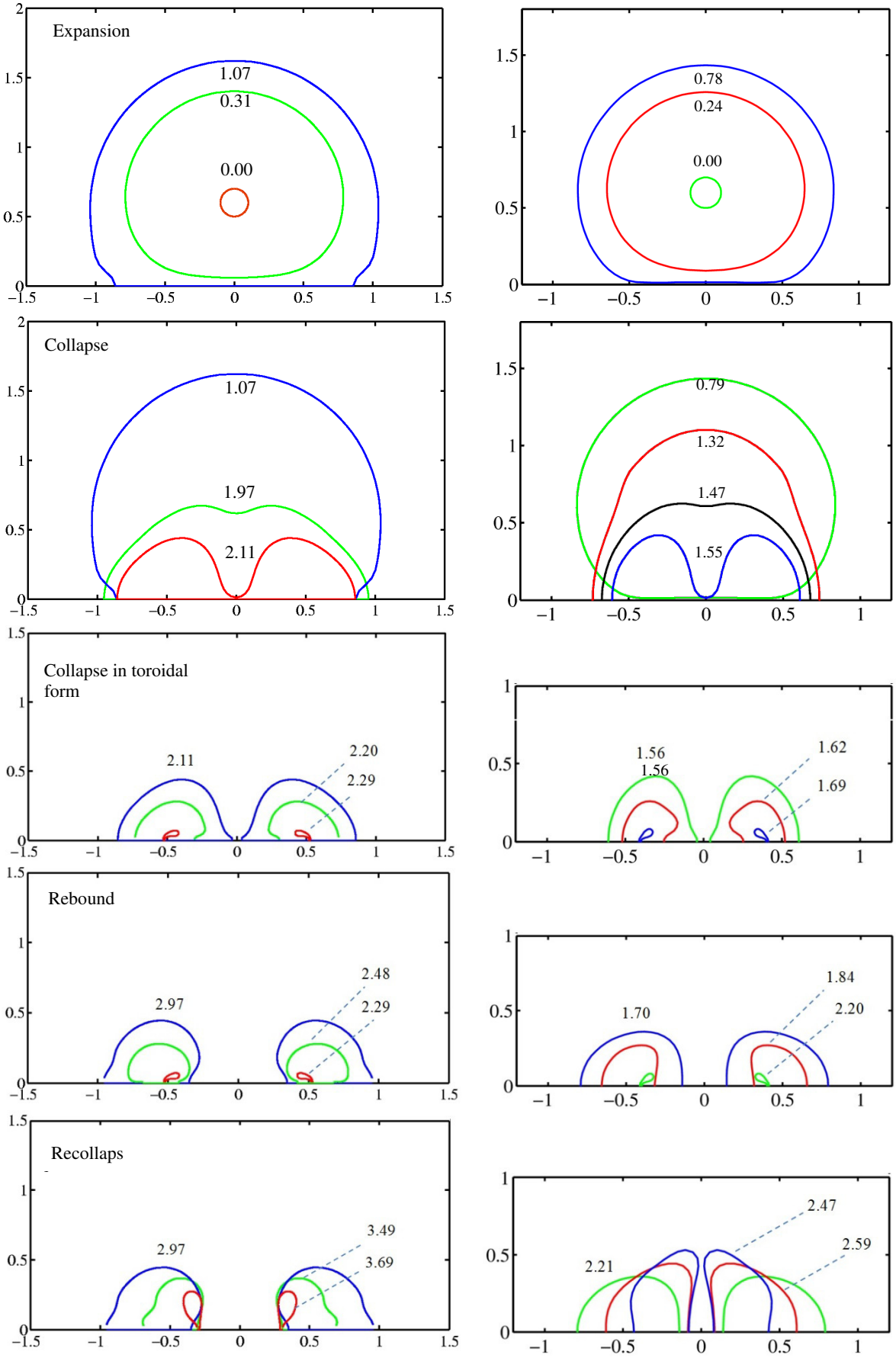
Expansion
1.07
0.31
0.00
0.78
0.24
0.00
Collapse
1.07
1.97
2.11
0.79
1.32
1.47
1.55
Collapse in toroidal form
2.11
2.20
2.29
1.56
1.56
1.62
1.69
Rebound
2.97
2.48
2.29
1.70
1.84
2.20
Recollaps
2.97
3.49
3.69
2.21
2.47
2.59

Figure 6. The bubble motion near a rigid boundary for $\gamma = 0.6$, and $R_{max} = 1.45$ mm ($Re = 1450$ and $\sigma_* = 0.00051$) (right column) and $R_{max} = 6$ μm ($Re = 60$ and $\sigma_* = 0.12$) (left column). The remaining parameters are the same as in figure 4.

Figure 7 shows the time histories of the equivalent bubble radius R_{eq*} for a bubble near a rigid boundary for the cases shown in figures 5 and 6, for $R_{max} = 6$ μm, 1.45 mm, and $\gamma = 0.9$, 0.6, respectively. For all the four cases, the maximum radius and period of oscillation decrease significantly from the first cycle to the second cycle of oscillation. The maximum radius and the period for $R_{max} = 6$ μm decrease more from the first to second cycle than that for $R_m = 1.45$ mm, since the former is associated with the viscous effects. However, from the second to the third cycle, maximum radius for $R_{max} = 6$ μm decreases less.

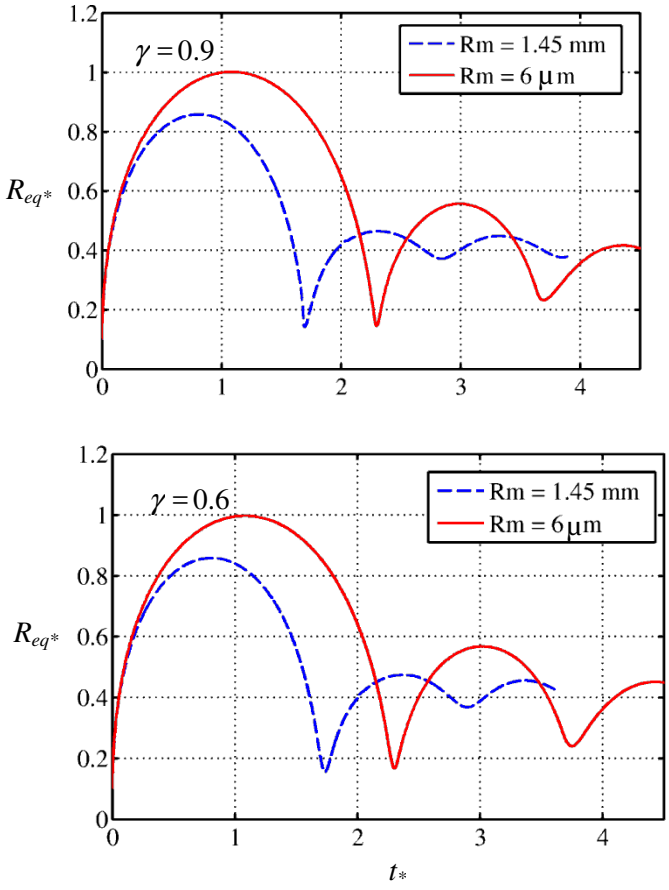

Figure 7. Time histories of the equivalent bubble radius R_{eq*} for a bubble near a rigid boundary for the cases in figures 5 and 6, for $R_{max} = 6$ μm, 1.45 mm, and $\gamma = 0.9$, 0.6, respectively.

Figure 8 shows the corresponding time histories for the local energy. The local energy deceases about 40% at the inception of the bubble for all the four cases, which is corresponding to the emission of a shockwave. At inception, the bubble size is small and relatively far away from the rigid boundary, the emission of shockwave does not depend on the standoff distance significantly. The viscous effects during the short period of the emission of shockwave are negligible too. The local energy for R_m = 1.45 mm remains almost constant before the end of collapse, since the associated Reynolds number is large. However the local energy for R_{max} = 6 μm decreases gradually during oscillation. At the end of collapse, the local energy decrease significantly for both of the two cases, when another shockwave is emitted. The bubble for R_{max} = 1.45 mm is associated with larger local energy before the shockwave emission and is thus associated with stronger collapse, stronger shockwave and larger energy loss.

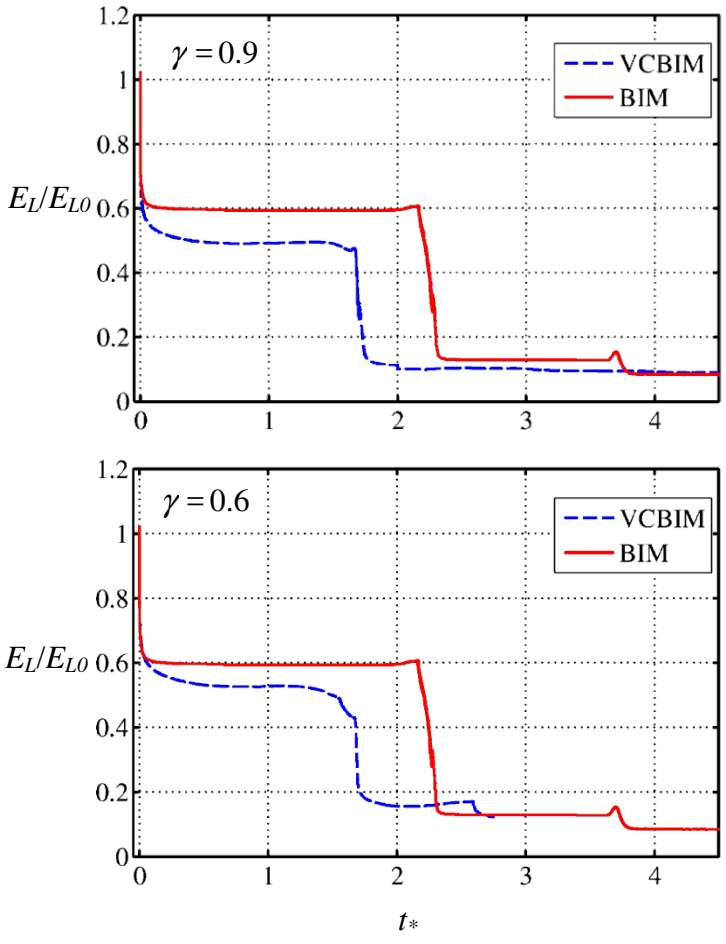

Figure 8. Time histories of the local energy for a bubble near a rigid boundary for the cases in figures 5 and 6, for R_{max} = 6 μm, 1.45 mm, and γ = 0.9, 0.6, respectively.

.

5. Summary and conclusions

Bubble dynamics near a rigid boundary are modelled using the weakly compressible theory and viscous potential flow theory coupled with the boundary integral method (BIM). Our computations correlate well the experimental data for both the first- and second-cycles of oscillation and the computations based on the Navier-Stokes equation.

The energy of a bubble system decreases due to both the compressible effects and viscous effects. At the inception of a bubble, the energy of a bubble system loses significantly for a very short time period, which is associated with the emission of a shockwave. This part of energy loss does not depend on the viscous effects and the presence of a rigid boundary. This is because the bubble size at inception is small and relatively far away from the rigid boundary, the emission of shockwave does not depend on the standoff distance significantly. The viscous effects during the short period of emission of shockwave are negligible too.

If the Reynolds number is large, the energy remains constant during the most part of oscillation period, where the compressible effects are negligible. If the Reynolds number is not large, the energy loses gradually during oscillation due to the viscous effects. The dimensionless oscillation period and the maximum bubble radius thus decrease due to viscous effects (i.e. increase with the Reynolds number).

The sharpness of the jet, the bubble volume at the jet impact, and the radius of the bubble ring formed at the end of collapse decrease with the viscous effects. At the end of collapse, the energy deceases rapidly and significantly, when another shockwave emits. For a smaller Reynolds number, a weaker shockwave is emitted at the end of collapse, since more energy losses during the first oscillation period. The radius of the bubble ring formed during recollapse is smaller than that during collapse.

Acknowledgements

This work was supported by the Engineering and Physical Sciences Research Council (EPSRC) through Grant No. EP/P015743/1.

References

Blake, J.R. (1999) Preface to Acoustic cavitation and sonoluminescence. Phil. Trans. R. Soc. Lond. A, 357, 201-201.

Blake, J. R. and Gibson, D. C. (1987) Cavitation bubbles near boundaries. Annual. Rev. Fluid Mech. 19 (1), 99-123.

Best, J. P. 1993 The formation of toroidal bubbles upon collapse of transient cavities. J. Fluid Mech. 251, 79–107.

Blake, J. R., Taib, B. B. and Doherty, G. (1986) Transient cavities near boundaries. Part 1. Rigid Boundary. J. Fluid Mech. 170, 497.

Blake, J. R., Taib, B. B. and Doherty, G. (1987) Transient cavities near boundaries. Part 2. Free surface. J. Fluid Mech. 181, 197.

Boulton-Stone, J. M. & Blake, J. R. 1993 Gas bubbles bursting at a free surface. 254, 437–466.

Chen, C., Gu, Y., Tu, J., Guo, X. and Zhang, D. (2016) Microbubble oscillating in a microvessel filled with viscous fluid: A finite element modeling study. Ultrasonics 66, 54-64.

Coussios, C., Roy, R.A. (2008) Applications of acoustics and cavitation to noninvasive therapy and drug delivery. Ann. Rev. Fluid Mech. 40, 395-420.

Curtiss, G. A., Leppinen, D.M., Wang, Q.X. and Blake, J.R. (2013) Ultrasonic cavitation near a tissue layer," J. Fluid Mech. 730 245-272.

Han, B., Köhler, K., Jungnicke, K., Mettin, R., Lauterborn, W. and Vogel A. (2015) Dynamics of laser-induced bubble pairs. J. Fluid Mech. 771, 706-742.

Hua, J. and Lou,J. (2007) Numerical simulation of bubble rising in viscous liquid. Journal of Computational Physics, 222(2), 769-795.

Hung, C. F. and Hwangfu, J. J. (2010) Experimental study of the behavior of mini-charge underwater explosion bubbles near different boundaries. J. Fluid Mech. 651, 55–80.

Klaseboer, E., Manica, R., Chan, D.Y.C., Khoo, B.C. (2011) BEM simulations of potential flow with viscous effects as applied to a rising bubble. Engg. Analysis Boundary Elements, 35, 489-494.

Kim, S. J., Lim, K. H. and Kim, C. (2006) Deformation characteristics of spherical bubble collapse in Newtonian fluids near the wall using the finite element method with ALE formulation. Korea Australia Rheology Journal, 18(2), 109-118.

Joseph, D.D. and Wang, J. (2004) The dissipation approximation and viscous potential flow. J. Fluid Mech., 505, 365-377.

Lauterborn, W. and Kurz, T. (2010) Physics of bubble oscillations. Rep. Prog. Phys. 73, 10650.

Lauterborn, W. and Vogel, A. (2013) Shock wave emission by laser generated bubbles. In Bubble Dynamics & Shock Waves (ed. C.F. Delale), 67-103. Springer-Verlag Berlin Heidelberg.

Lezzi, A. & Prosperetti, A. (1987) Bubble dynamics in a compressible liquid. Part. 2. Second-order theory. J. Fluid Mech. 185, 289–321.

Lind, S.J. and Phillips, T.N. (2010) The effect of viscoelasticity on a rising gas bubble. Journal of non-Newtonian fluid mechanics 165(15-16),852-865.

Lind, S.J. and Phillips, T.N. (2012) The influence of viscoelasticity on the collapse of cavitation bubbles near a rigid boundary. Theoret. & Comput. Fluid Dyn. 26(1-4), 245-277.

Lind, S.J. and Phillips, T.N. (2013) The effect of viscoelasticity on the dynamics of gas bubbles near free surfaces. Physics of Fluids 25(2),022104-022135.

Liu, Y.L., Wang, S.P., Wang, Q.X. and Zhang, A.M. (2016) 3D toroidal bubble dynamics and its interaction with a free surface near an inclined wall. Physics of Fluids 28, 122101, doi: 10.1063/1.4972771.

Manmi,K. and Wang Q.X. (2017) Acoustic microbubble dynamics with viscous effects. Ultrasonics Sonochemistry 36, 427-436.

Minsier, V.J., Wilde, De. and Proost, J. (2009) Simulation of the effect of viscosity on jet

penetration into a single cavitating bubble. Journal of Applied Physics, 106(8), 084906.

Ohl, C.D., Arora, M., Dijkink, R., Janve, V., Lohse, D. (2006) Surface cleaning from laserinduced cavitation bubbles. Applied physics letters 89(7), 074102.

Philipp, A. and Lauterborn, W. (1998) Cavitation erosion by single laser-produced bubbles. J. Fluid Mech. 361, 75–116. (doi: http://dx.doi.org/10.1017/S0022112098008738)

Popinet, S. and Zaleski, S. (2002) Bubble collapse near a solid boundary: a numerical study of the influence of viscosity. J. Fluid Mech. 464, 137-163.

Prosperetti, A. & Lezzi, A. (1986) Bubble dynamics in a compressible liquid. Part 1. First-order theory. J. Fluid Mech. 168, 457–478.

Reuter, F., Lauterborn, S., Mettin, R. and Lauterborn, W. (2017) Membrane cleaning with ultrasonically driven bubbles. Ultrasonics Sonochemistry 37, 542–560.

Suslick, K.S. (1990) Sonochemistry. Science 247, 1439–1445. Tiwari, A., Freund, J. B. and Pantano, C. (2013) A Diffuse Interface Model with Immiscibility Preservation. J. Comput. Phys. 252, 290-309.

Vyas, N., Pecheva, E., Dehghani, H., Sammons, R.L., Wang, Q.X., Leppinen, D.M. and Walmsley A.D. (2016) High speed imaging of cavitation around dental ultrasonic scaler tips. PLOS ONE 11(3): e0149804.

Vyas, N., Dehghani, H., Sammons, R.L., Wang, Q.X., Leppinen, D.M. and Walmsley A.D. (2017) Imaging and analysis of individual cavitation microbubbles around dental ultrasonic scalers. Ultrasonics, 81, 66-72.

Wang, Q. X. (1998) The numerical analyses of the evolution of a gas bubble near an inclined wall. Theoret. & Comput. Fluid Dyn. 12, 29-51.

Wang, Q. X. (2004) Numerical modelling of violent bubble motion. Phys. Fluids 16 (5), 1610-1619.

Wang, Q. X. (2013) Underwater explosion bubble dynamics in a compressible liquid. Phys. Fluids, 25, 072104.

Wang, Q. X. (2016) Local energy of a bubble system and its loss due to acoustic radiation. Journal of Fluid Mechanics, 797, 201–230.

Wang, Q. X. and Blake J.R. (2011) Non-spherical bubble dynamics in a compressible liquid. Part 2. Standing acoustic wave. J. Fluid Mech., 679, 559-581.

Wang, Q. X. and Blake J.R. (2010) Non-spherical bubble dynamics in a compressible liquid. Part 1. Travelling acoustic wave. J. Fluid Mech., 659, 191-224.

Wang, Q.X., Liu, W.K., Zhang A. and Sui, Y (2015a) Bubble dynamics in very close to a rigid boundary. Interface Focus, 5(5), 20150048. DOI: 10.1098/rsfs.2015.0048.

Wang, Q. X., Manmi, K. and Liu, K.K. (2015b) Cell mechanics in biomedical cavitation. Interface Focus, 5(5) 20150018. DOI: 10.1098/rsfs.2015.0018.

Wang, Q. X., Yeo, K. S., Khoo, B. C. and Lam, K. Y. (1996a) Nonlinear interaction between gas bubble and free surface. Comput. & Fluids 25 (7), 607.

Wang, Q. X., Yeo, K. S., Khoo, B. C. and Lam, K. Y. (1996b) Strong interaction between buoyancy bubble and free surface. Theor . Comput. Fluid Dyn. 8, 73.

Wang, Q. X., Yeo, K. S., Khoo, B. C. and Lam, K. Y. (2005) Vortex ring modelling for toroidal bubbles. Theoret. & Comput. Fluid Dyn. 19 (5), 303-317.

Smith, W.R. and Wang, Q. X. 2017 Viscous decay of nonlinear oscillations of a spherical bubble at large Reynolds number. Phys. Fluids 29, 082112.

Smith, W.R. and Wang, Q. X., 2017 Radiative decay of the nonlinear oscillations of an adiabatic spherical bubble at small Mach number. J. Fluid Mech. (in print).

Zhang, A.M. and Ni, B.Y. (2014) Three-dimensional boundary integral simulations of motion and deformation of bubbles with viscous effects. Comput. & Fluids 92, 22-33.

Zhang, S. G. and Duncan, J. H. (1994) On the nonspherical collapse and rebound of a cavitation bubble. Phys. Fluids 6 (7), 2352–2362.

Zhang, S. G., Duncan, J. H., and Chahine G. L. (1993) The final stage of the collapse of a cavitation bubble near a rigid wall. J. Fluid Mech. 257, 147-181.